Check for updates

The role of Cu_1–O_3 species in single-atom Cu/ZrO_2 catalyst for CO_2 hydrogenation

Huibo Zhao[1], Ruofan Yu[1], Sicong Ma [2], Kaizhuang Xu[1], Yang Chen[1], Kun Jiang[1], Yuan Fang[1], Caixia Zhu[1], Xiaochen Liu[1], Yu Tang [1], Lizhi Wu[1], Yingquan Wu[3], Qike Jiang[4], Peng He[3,5], Zhipan Liu [2,6] ✉ and Li Tan [1] ✉

Copper-based catalysts for the hydrogenation of CO_2 to methanol have attracted much interest. The complex nature of these catalysts, however, renders the elucidation of their structure–activity properties difficult. Here we report a copper-based catalyst with isolated active copper sites for the hydrogenation of CO_2 to methanol. It is revealed that the single-atom Cu–Zr catalyst with Cu_1-O_3 units contributes solely to methanol synthesis around 180 °C, while the presence of small copper clusters or nanoparticles with Cu–Cu structural patterns are responsible for forming the CO by-product. Furthermore, the gradual migration of Cu_1-O_3 units with a quasiplanar structure to the catalyst surface is observed during the catalytic process and accelerates CO_2 hydrogenation. The highly active, isolated copper sites and the distinguishable structural pattern identified here extend the horizon of single-atom catalysts for applications in thermal catalytic CO_2 hydrogenation and could guide the further design of high-performance copper-based catalysts to meet industrial demand.

The excessive use of fossil fuels in recent decades has led to a dramatic increase in the amount of CO_2 in the atmosphere, which has caused serious damage to the natural environment. Hence, the related C1 chemistry has become an important research area because one of the most challenging scientific issues is to find alternative energy sources to replace petroleum in the 21st century[1]. In particular, the industrial conversion of excess CO_2 into high-value-added chemicals and energy fuels can not only effectively mitigate the greenhouse effect, but also represents a sustainable use of natural resources[2–7]. Methanol (CH_3OH), as a basic industrial raw material, can be used to synthesize a series of important industrial chemicals, such as low-carbon olefins and gasoline[8–13]. It is thus obvious that the process of CH_3OH catalysis from CO_2 is of great commercial value. Therefore, in the past few decades, much research has been performed to find catalysts with good performance, including metal–metal oxides ($Cu/ZnO/Al_2O_3$ (refs. [14,15]), Cu/In_2O_3 (ref. [16]), Cu/ZrO_2 (refs. [17–19]), Pd/ZnO (ref. [20])), metal-oxide solid solutions (ZnO/ZrO_2 (ref. [21]), In_2O_3/ZrO_2 (ref. [22]), $CdZrO_x$ (ref. [23])) and metal alloys (Ni_xGa_y (ref. [24]), Pd_xGa_y (ref. [25]), Pt_xCo_y (ref. [26]), etc.).

Among CO_2 hydrogenation catalysts, copper catalysts have attracted much attention because of their excellent catalytic activity and stability for CH_3OH synthesis[19,27]. However, the actual active sites for various products in copper-based catalysts are difficult to pinpoint due to the complex coordination structure of copper species. The diversity of valence states of copper species and the particularity of hydrogenation reactions means that copper mostly exists in mixed valence states during these reactions. There are conflicting reports in the literature showing that either Cu^0, Cu^+ or $Cu^{\delta+}$ may be active sites[18,19,28,29]. Moreover, the physical size of copper nanoparticles also profoundly affects the catalytic performance[17,30–33]. These different factors have a great impact on the coordination structure of copper itself, which makes it difficult to study the actual active copper sites for CO_2 hydrogenation. Although substantial progress has been made in understanding the active sites of copper catalysts, there is still much controversy about the structure–performance correlation between catalyst and reaction[18,32,34–36].

For the above reasons, catalysts with stable and uniform sites are necessary for the study of related catalytic structure–activity relationships. The single-atom catalyst is an ideal model for active sites study due to its uniform metal sites which are embodied in the homogeneous catalyst[37–39]. However, such work is rarely reported because it is difficult to construct effective and stable active sites in the thermal catalytic hydrogenation of CO_2 to CH_3OH (refs. [33,40–42]). Here we synthesized an efficient Cu_1/ZrO_2 single-atom catalyst to realize the CO_2 hydrogenation reaction to CH_3OH at relatively low temperature (180 °C). Compared to typical Cu/ZrO_2 catalysts, the monoatomic dispersed Cu_1/ZrO_2 displayed a higher turnover frequency (TOF) for CH_3OH and 100% CH_3OH selectivity. Starting from the structure of the monatomic catalyst model, the relationship between the structure of active copper sites and the formation of methanol or CO is explored in depth.

Results
The design of copper catalysts with different structure models. A series of Cu/ZrO_2 catalysts with different copper loadings (1–15 wt%) were synthesized by a modified co-precipitation and impregnation method. The copper-based amorphous/monoclinic ZrO_2

¹Institute of Molecular Catalysis and In Situ/Operando Studies, State Key Laboratory of Photocatalysis on Energy and Environment, College of Chemistry, Fuzhou University, Fuzhou, China. ²Key Laboratory of Synthetic and Self-Assembly Chemistry for Organic Functional Molecules, Shanghai Institute of Organic Chemistry, Chinese Academy of Sciences, Shanghai, China. ³State Key Laboratory of Coal Conversion, Institute of Coal Chemistry, Chinese Academy of Sciences, Taiyuan, China. ⁴Dalian National Laboratory for Clean Energy, Dalian Institute of Chemical Physics, Chinese Academy of Sciences, Dalian, China. ⁵National Energy Research Center for Clean Fuels, Synfuels China Co., Ltd., Beijing, China. ⁶Shanghai Key Laboratory of Molecular Catalysis and Innovative Materials, Key Laboratory of Computational Physical Science, Department of Chemistry, Fudan University, Shanghai, China. ✉e-mail: zpliu@fudan.edu.cn; tan@fzu.edu.cn

with different amounts of copper (x wt%) were named CAZ-x and CMZ-x, respectively. The actual copper concentration in various Cu/ZrO$_2$ samples was measured by inductively coupled plasma optical emission spectrometry (ICP-OES) (Supplementary Table 1). As shown in Supplementary Fig. 1a, all the Cu/a-ZrO$_2$ catalysts with different copper loading amounts exhibited an amorphous state of ZrO$_2$ and no X-ray diffraction peaks of CuO species, suggesting that the copper species were highly dispersed on a-ZrO$_2$ (ref. [43]). The similar specific surface areas and pore structures also indicated a high degree of dispersion of copper species (Supplementary Table 2). Notably, a-ZrO$_2$ transformed to tetragonal phase without adding Cu^{2+} precursor during the same co-precipitation procedure (Supplementary Fig. 1b). The change in phase indicated that a strong interaction effect existed between copper and ZrO$_2$. The broad Raman spectroscopy peak at 523 cm^{-1} also confirmed amorphous zirconia was formed in Cu/a-ZrO$_2$ catalysts with various copper loadings (Supplementary Fig. 2)[44].

To confirm the hyperfine structure of the Cu/a-ZrO$_2$ catalysts at the atomic scale, high-angle annular dark-field scanning transmission electron microscopy (HAADF-STEM) and X-ray absorption spectroscopy (XAS) were used. The HAADF-STEM images of CAZ-1 (Fig. 1a and Supplementary Fig. 3) showed that the sample consisted of a-ZrO$_2$ with no copper species nanoparticles on it. Elemental mapping (Fig. 1d) also confirmed highly dispersed copper sites were located in the CAZ-1 catalyst, consistent with the XRD and HAADF-STEM results. For copper loading amounts of up to 15 wt%, the copper species remained highly dispersed on the ZrO$_2$ substrate (Fig. 1b and Supplementary Fig. 4). Extended X-ray absorption fine structure (EXAFS) spectroscopy in R space and corresponding wavelet transform (WT) spectra supplied more important information about the structure of the catalysts, as shown in Fig. 1g,h and Supplementary Fig. 5a. Only one apparent peak at 1.92 Å corresponding to the first coordination shell of Cu–O scattering could be detected in CAZ-1 and CAZ-15. This provided evidence that copper sites were atomically dispersed in CAZ-1 and CAZ-15 because no Cu–(O)–Cu or Cu–Cu metallic bonds were observed[45]. It is difficult to completely exclude copper single atoms by just increasing the copper loading in CAZ-x catalysts due to the unique molecular interactions between copper and a-ZrO$_2$. Therefore, catalysts containing 15 wt% copper were synthesized with CuO nanoparticles over monoclinic ZrO$_2$ substrate (CMZ-15) and bare Q50 (SiO$_2$) (CS-15), and served as reference catalysts. The obvious X-ray diffraction peaks at 35.5° and 38.7° (Supplementary Fig. 6a,b) and the Raman peak at 291 cm^{-1} (Supplementary Fig. 2) correspond to the existence of CuO nanoparticles[46]. The highly agglomerated CuO particles were also observed in the CMZ-15 (15–30 nm) and CS-15 (~0.6 μm) catalysts from transmission electron microscopy (TEM) images and corresponding elemental mapping (Fig. 1c,f and Supplementary Fig. 7a–j). Moreover, an additional smaller peak corresponding to CuO at 2.81 Å was observed in EXAFS and WT spectra (Fig. 1g, Supplementary Fig. 5b), ascribed to Cu–(O)–Cu scattering at the second shell, confirming the formation of CuO particles[47]. In summary, the copper species existed as single atoms and large CuO particles in the CAZ-x (x = 1–15 wt%) series catalysts and CMZ-15 samples, respectively.

Catalytic performance for CO$_2$ hydrogenation. The catalytic performance of Cu/ZrO$_2$ catalysts for hydrogenation of CO$_2$ to CH$_3$OH was evaluated at 180 °C and 3 MPa with CO$_2$/H$_2$ mixed gas (CO$_2$:H$_2$ = 1:3). Prior to reaction, CAZ-x (x = 1–15 wt%) catalysts were pretreated at 230 °C for 10 h under an argon atmosphere. CAZ-1, CMZ-15 and CS-15 were pretreated at 300–370 °C under a hydrogen atmosphere to form metallic copper particle species. The CO$_2$ conversion over all the catalysts was controlled to less than 10% to study their intrinsic activity, which was far lower than the CO$_2$ equilibrium conversion under reaction conditions

(29.7% at 180 °C; Supplementary Fig. 8). As shown in Fig. 2a,b and Supplementary Table 3, using CAZ-1 resulted in the detection of only CH$_3$OH, and no by-products, and this catalyst preferentially produced CH$_3$OH with a TOF$_{Cu}$ value of up to 1.37 h^{-1}. We have therefore synthesized a 'homogeneous' active site catalyst with excellent stability for CH$_3$OH production from CO$_2$ hydrogenation. However, CO$_2$ could not be activated by CAZ-1-r (CAZ-1 pre-reduced by H$_2$ at 370 °C to form large copper particles), CMZ-15 and CS-15 catalysts, according to the high aggregation of copper species into large particles, confirmed by the X-ray diffraction results (Supplementary Figs. 6a,b and 9) and H$_2$ temperature programmed reduction (TPR) (Supplementary Fig. 10b). Therefore, the highly dispersed, isolated copper species might be the actual active sites for CH$_3$OH synthesis from CO$_2$ at low temperatures. Compared with the Cu/ZrO$_2$ catalysts reported previously in the literature, the CAZ-1 with single-atom copper sites in this work offers advantageous catalytic performance for methanol synthesis (Supplementary Table 4). As the copper amount increases in the CAZ-x catalysts (Fig. 2c), CO starts to be produced from CAZ-4 catalyst, indicating additional active sites were formed in these high-copper-loading catalysts (Supplementary Fig. 11) during the reaction process. It was inferred that the copper clusters or small nanoparticles that form on CAZ-x catalysts (>4 wt% Cu) played a crucial role in accelerating reverse water gas shift (RWGS) reaction since no activity was observed over CAZ-1-r, CMZ-15 and CS-15 catalysts with large metallic copper particles. These catalysts exhibited excellent intrinsic activity in the low loading range (<2 wt% Cu). A good linear growth relationship of CO$_2$ conversion was observed for CAZ-1, CAZ-1.5, CAZ-2 and CAZ-2.5, with only CH$_3$OH being produced (Supplementary Fig. 12a). The ratios of R$_x$/R$_1$ (R$_x$ = CO$_2$ conversion/actual copper loading, x = 1.5, 2, 2.5, 4) for CAZ-1.5/CAZ-1, CAZ-2/CAZ-1, CAZ-2.5/CAZ-1 and CAZ-4/CAZ-1 are 0.99, 0.96, 0.97 and 0.67, respectively, indicating that the active copper sites were uniformly dispersed and exposed on the catalysts' surface in the single-atom state in CAZ-x (x = 1–2.5). However, the increasing trend of conversion rate decreased for copper contents higher than 4 wt% (R$_4$/R$_1$ = 0.67), since the copper clusters could not provide CO$_2$ activation ability as strong as that of isolated active copper sites, and hence the CO selectivity was much lower than the CH$_3$OH selectivity. When the copper loading amount was more than 8 wt%, the surface of the catalyst was filled up with copper clusters and isolated Cu$^{δ+}$ sites at the same time as large particles of Cu^0—which have no CO$_2$ activation ability—gradually formed (Supplementary Fig. 12b), resulting in no further increase of the CO$_2$ conversion due to the saturation of surface-active sites.

Further evidence for this mechanism is provided by the catalytic performance and ICP-OES results (Supplementary Table 1) of CAZ-15-H (where CAZ-15-H is CAZ-15 pretreated with HNO$_3$ for 20 h), where the large copper nanoparticles were partially removed. The catalytic performance was similar to that of CAZ-8–15 and the actual copper loading amount was close to that of CAZ-8, indicating that the effective active sites of copper species on a-ZrO$_2$ surface comprised about 7–8 wt%. In addition, we also proved that the active sites in the catalyst were in a very stable structure that even strong acid could not break. CAZ-1 was also tested in the CO$_2$ conversion reaction continuously for 100 h to evaluate its catalytic stability (Fig. 2d and Supplementary Fig. 13a,b). After an induction period of a couple of hours, the catalyst with isolated active copper sites gave both very stable CO$_2$ conversion and target product selectivity, demonstrating that the catalyst possesses an extremely stable structure in the CO$_2$ hydrogenation reaction. Furthermore, fresh and used CAZ-1 catalysts had similar weight loss and heat absorption/exothermic trends, indicating that CAZ-1 has a stable structure with no carbon deposition on its surface during low-temperature reaction (Supplementary Fig. 14).
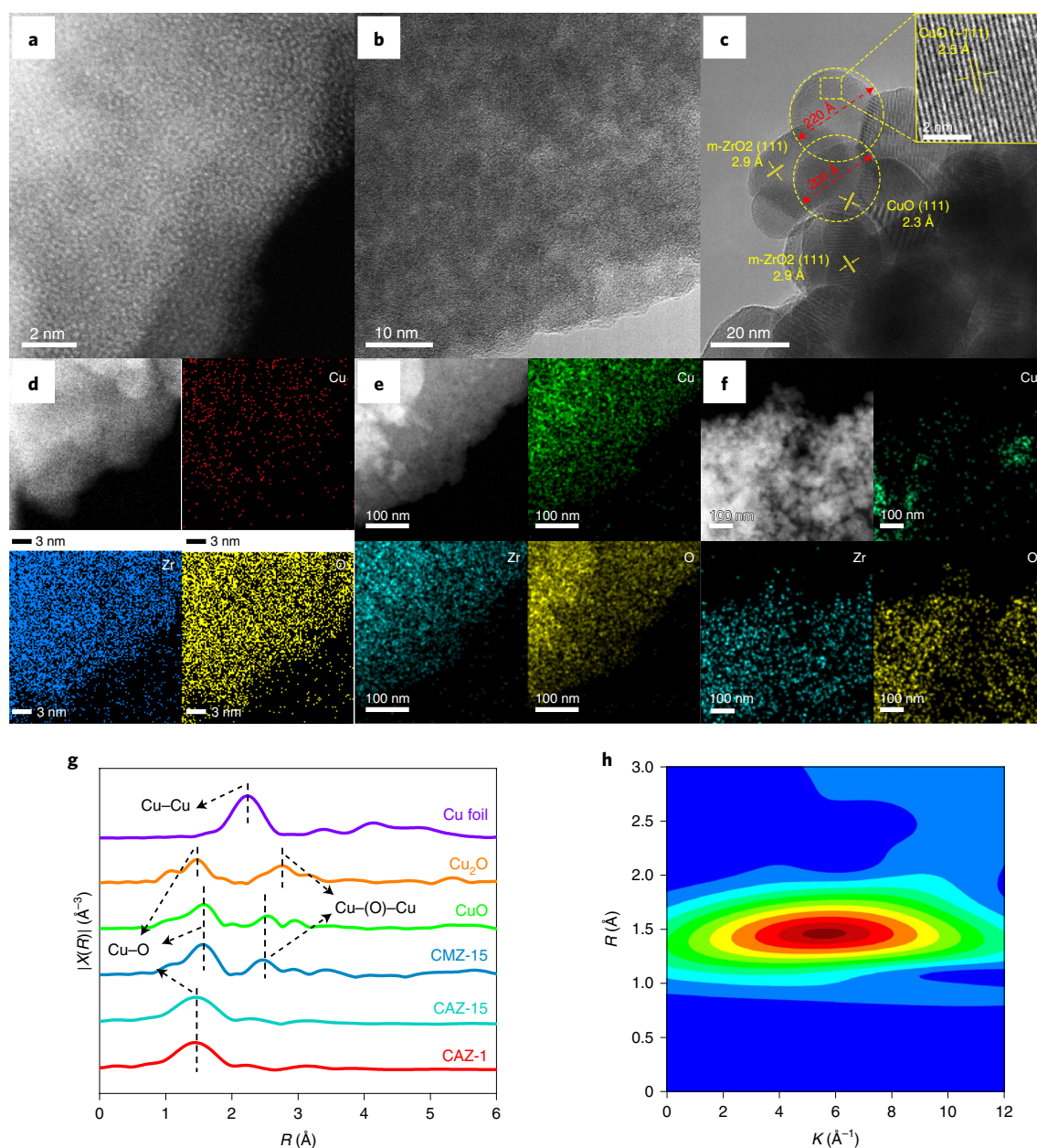
Fig. 1 | Characterization of different Cu/ZrO₂ catalysts. a–f, HAADF-STEM image and elemental mapping of CAZ-1 (**a,d**), and TEM image and elemental mapping of CAZ-15 (**b,e**) and CMZ-15 (**c,f**). **g,** The corresponding k^2-weighted Fourier transform spectra of as-prepared samples and references. **h,** The WT spectroscopy of CAZ-1.

Surface electronic state and coordination structure. The electronic state and short-range coordination environment of the catalysts were investigated to study their relationship to the catalytic performance. The Cu 2p species for CAZ-1 and CAZ-1-U (where U signifies used) were located at about 931.9 eV, and their Auger electron spectroscopy (AES) (Supplementary Fig. 15a,b) signals were located at 916.5 eV, indicating the presence of Cu⁺ in the samples before and after the reaction[48]. For the CAZ-15 sample, the content of Cu²⁺ species decreased significantly after the reaction (from 66% to 32%; Supplementary Table 5 and Supplementary Fig. 15a,b), indicating that the Cu²⁺ was partially in situ reduced to Cu⁰ during the reaction (Supplementary Fig. 12b). The coexisting Cu⁰ clusters or small particles and Cu⁸⁺ species in CAZ-15 convert CO₂ to CO and CH₃OH, respectively.

Because the accuracy of X-ray photoelectron spectroscopy (XPS) was insufficient while the copper species were highly dispersed with

low loading amounts[49–53], the valence state of catalysts was confirmed by X-ray absorption near-edge structure (XANES) measurements for more accurate investigations (Fig. 3a–d and Supplementary Fig. 16a–c). In comparison to the copper foil, the absorption edges for CAZ-1 and CAZ-1-U shifted to higher energy, indicating that the copper atoms were in an oxidized state (Fig. 3a). Peaks A (Cu²⁺, 8,978 eV, 1s → 3d), B (Cu²⁺, 8,985 eV, 1s → 4p) and C (Cu²⁺, 8,997 eV, 1s → 4p) were similar to those of CuO in the XANES spectrum (Fig. 3b), but the details were different (the intensity of these peaks, especially peak D at 9,010.8 eV, represent multiple scattering of Cu²⁺). This indicated that the valence of copper species in fresh and used CAZ-1 were close to 2+ (refs. [45,51,54]). To reflect the true valence information of copper species in CAZ-1 during the reaction process, an in situ XAS test was performed. As shown in Fig. 3a–c, the absorption edge and first derivative of CAZ-1 (in situ) was
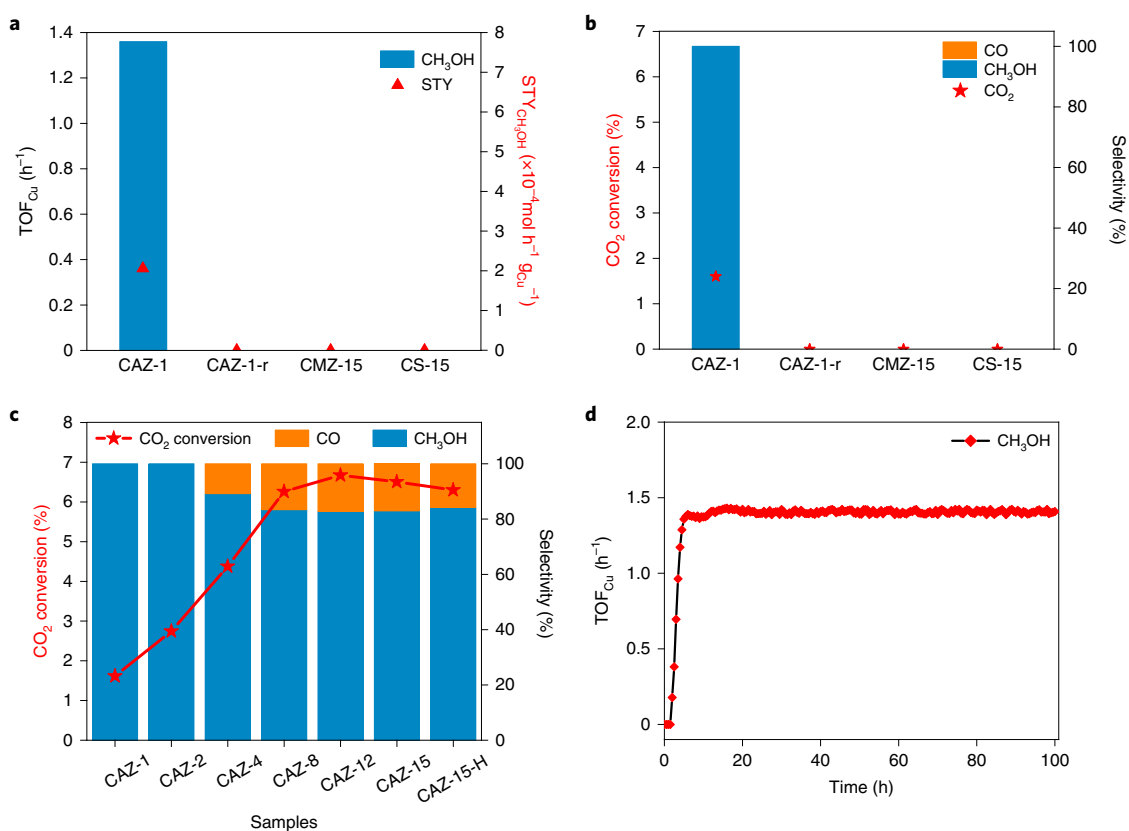
Fig. 2 | Catalytic performance of different copper-based catalysts. a, TOF_{Cu} values and space-time yield (STY) of CAZ-1, CMZ-15 and CS-15. **b**, CO_2 conversion and product selectivity of CAZ-1, CMZ-15 and CS-15. **c**, The catalytic activity of CAZ-x and CAZ-15-H. **d**, The stability test of CAZ-1. Reaction conditions: 0.5 g catalyst, 3 MPa, 180 °C, CO_2:H_2=1:3, 10 ml min^{-1}.

between Cu$^+$ and Cu^{2+}, suggesting the oxidation state of Cu$^{\delta+}$ ($1 < \delta < 2$) species. Based on the XANES spectra of copper foil, Cu_2O and CuO, the valence of Cu$^{\delta+}$ (in situ) was estimated to be ~1.4 according to our linear fitting results, as shown in Fig. 3d. Therefore, it was deduced that the valence of copper species in CAZ-1 and CAZ-1-U was close to 2+ but would be decreased to ~1.4+ during the CO_2 hydrogenation reaction. Although the fresh CAZ-15 also gave a similar XANES spectra as CAZ-1, the copper species would be changed into a different state during the reaction process, leading to their distinctly different catalytic performances (Supplementary Fig. 6c,d and Fig. 2c). As for CMZ-15, an apparent pre-edge peak at 8,984 eV was detected, which confirmed that the CuO particle was embodied in CMZ-15 (Supplementary Fig. 6c, d)[55], corresponding to the X-ray diffraction results (Supplementary Fig. 6a).

The EXAFS fitting data for Cu/ZrO$_2$ are shown in Fig. 3e–g, Supplementary Fig. 16d–j and Supplementary Table 6. The copper species in CAZ-1 remained monodispersed after the reaction, and the average Cu–O coordination numbers before and after the reaction were 2.84 and 2.72, respectively. Combined with the results of theoretical calculations ($Cu_1–O_3$ has the lowest surface potential; Supplementary Fig. 17), these data indicate that the local structure of CAZ-1 comprised one isolated copper atom coordinated with about three oxygen atoms ($Cu_1–O_3$ units) in a quasiplanar structure with an angle of about 11° between the copper and oxygen atoms on the a-ZrO$_2$ surface (Fig. 3h). Furthermore, in situ EXAFS was used to study the structure of CAZ-1 under operando conditions. The fitted data indicated that reduction of the copper species in CAZ-1 to metallic copper was difficult under the reaction conditions, which was consistent with the results of H$_2$-TPR (Supplementary

Fig. 10a, c), indicating that the copper species were still distributed in a single-atom state. The Cu–O coordination number slightly decreased to 2.56 during the reaction, accompanied by a slight decrease in the valence state. Meanwhile, the Cu–O bond became slightly longer under the reaction conditions (increasing from 1.92 to 2.05 Å; Supplementary Table 6), indicating that the $Cu_1–O_3$ sites were activated under the reaction conditions.

The active sites for copper-based catalysts. It was hypothesized that isolated $Cu_1–O_3$ sites might favour CO_2 conversion to CH_3OH. Because no copper particles were detected in the spent CAZ-1 (Fig. 4a and Supplementary Fig. 18a), we concluded that isolated $Cu_1–O_3$ active sites in Cu/ZrO$_2$ were in fact stable. However, the local copper particles with 0.21 nm spacing of the Cu(111) planes[16,56–58] detected in CAZ-15-U by HRTEM (Fig. 4b and Supplementary Fig. 18b) revealed that copper species were partially aggregated and reduced during the catalytic process, consistent with the X-ray diffraction results (Fig. 4c). H$_2$-TPR was also performed to elucidate the evolution of the copper species under a reduced atmosphere (Supplementary Fig. 10). The TPR results indicated that reduction of the Cu$^{\delta+}$ species in CAZ-1 was difficult: only one peak at 360 °C appeared, which was much higher than the actual reaction temperature, indicating the stability of $Cu_1–O_3$ active sites. As the copper content increased from 1 wt% to 15 wt%, this reduction peak shifted to lower temperatures, demonstrating that the interaction between the copper species and ZrO$_2$ carrier gradually weakened. The explanation for this behaviour is that the copper species is more easily aggregated and thereby further reduced as its loading amount increased. The X-ray diffraction results (Fig. 4c and Supplementary Fig. 12b) also supported this hypothesis:
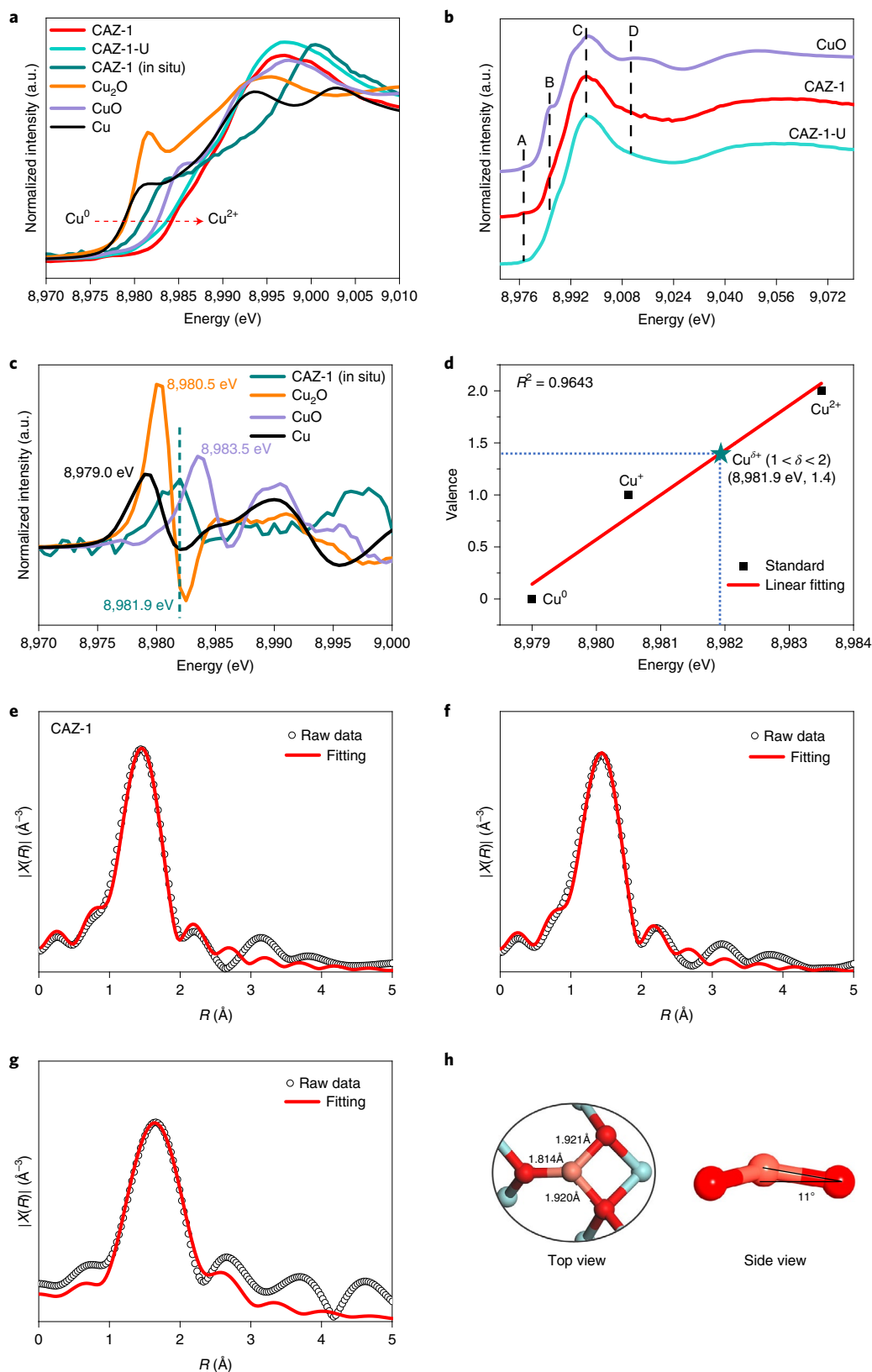
Fig. 3 | Electronic property and structure of CAZ-1. a, Cu K-edge XANES spectra of Cu/ZrO₂ and standards. **b**, Comparison of XANES spectra of CAZ-1, CAZ-1-U and CuO standard. **c**, The first derivatives of XANES spectra of CAZ-1 (in situ) and reference materials. **d**, The mean chemical valence of Cu$^{\delta+}$ species in CAZ-1 under in situ test conditions. **e–g**, Fitting of k^2-weighted EXAFS data of CAZ-1 (**e**), CAZ-1-U (**f**) and CAZ-1 (in situ) (**g**) in the region of 1.0–3.0 Å. **h**, The proposed Cu₁–O₃ configuration of CAZ-1. The in situ XAS test condition: sample was pretreated with pure argon (30 ml min⁻¹) at 230 °C for 2 h, then cooled down to 180 °C and treated in mixed gas (CO₂:H₂ = 1:3) at 1 MPa. The gas flow was then adjusted to 10 ml min⁻¹ and the data recorded.
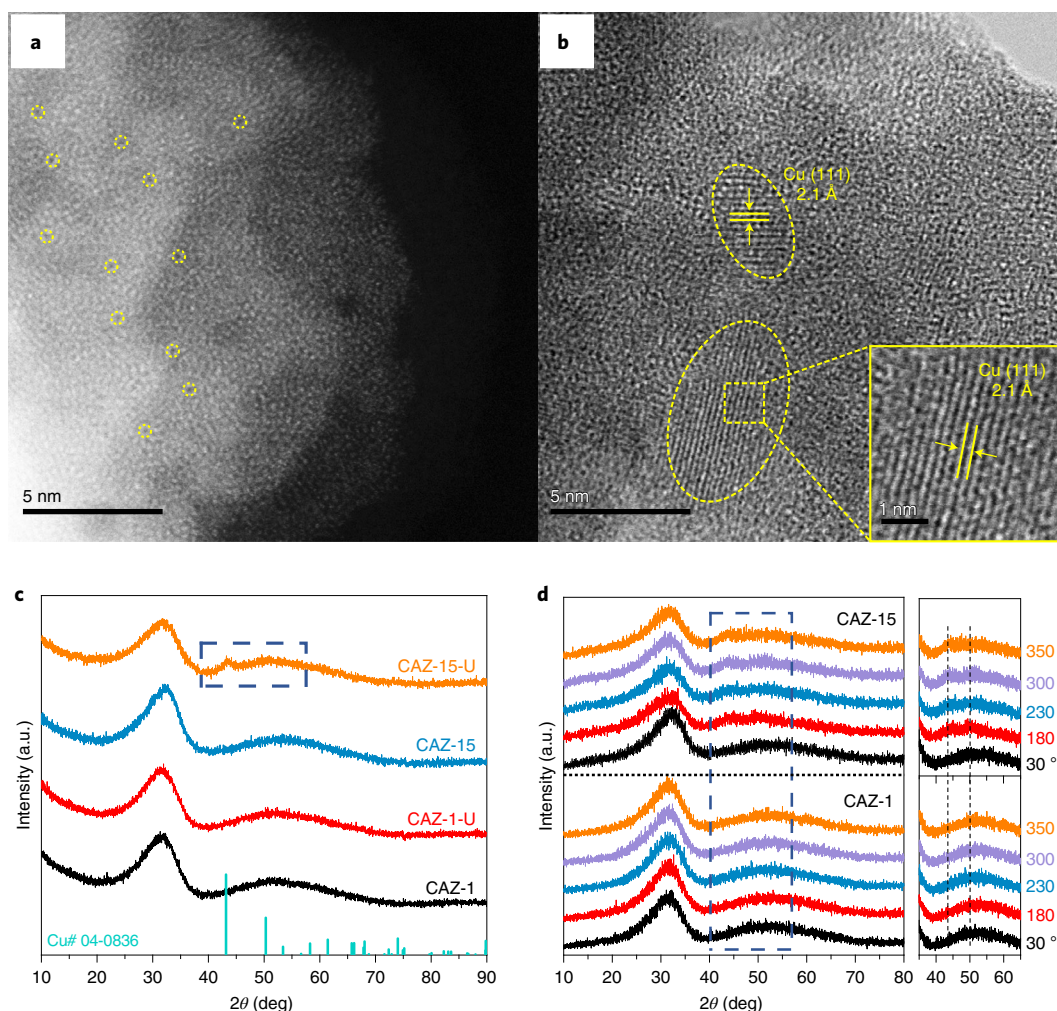
Fig. 4 | Morphology and crystal structure of different Cu/a-ZrO$_2$ catalysts. a, HAADF-STEM image of CAZ-1-U. Black spots in the yellow circles may be single copper atoms or background. **b**, HRTEM image of CAZ-15-U. **c**, X-ray diffraction profiles of CAZ-1, CAZ-1-U, CAZ-15 and CAZ-15-U ("04-0836" is the standard card of copper metal). **d**, In situ X-ray diffraction profiles for different Cu/a-ZrO$_2$ under pure hydrogen.

no copper particle diffraction peaks were detected and the crystal structure remained in the amorphous state for used CAZ-1 catalyst. In contrast, two obvious sharp peaks (43.3° and 50.4°)[59,60] appeared in used CMZ-15 and CS-15, suggesting the formation of copper from CuO reduction (Supplementary Fig. 6), which was corroborated by TEM (Supplementary Figs. 19 and 20). Furthermore, in situ X-ray diffraction was employed to investigate the dynamic evolution of Cu$^{\delta+}$ species in Cu/a-ZrO$_2$ under a hydrogen atmosphere. As shown in Fig. 4d, no signal of Cu^0 was observed in CAZ-1 catalyst with increasing temperature ($30 \rightarrow 180 \rightarrow 230 \rightarrow 300 \rightarrow 350$ °C). However, for CAZ-15, two faint signals at 43.3° and 50.4° appeared, and the intensity of these gradually increased as the temperature increased from 180 to 350 °C in a hydrogen atmosphere. Therefore, the Cu^{2+} species in CAZ-15 were partially reduced at 180 °C and high temperatures could further increase their degree of reduction. H$_2$ temperature-programmed desorption (TPD) (Supplementary Fig. 21) showed peaks at ~420 °C that were assigned to sites of H$_2$ absorption at copper species and a-ZrO$_2$ substrate. Compared with CAZ-1, the corresponding peak in CAZ-15 migrated to a higher temperature (415 °C $\rightarrow$ 430 °C), possibly caused by the greater number of supplied adsorption sites on the CAZ-15 surface, indicating that the structure of copper species in CAZ-15 was more complex and non-unique. Based on the above results, it was concluded that the dispersion of copper species in CAZ-1 was still in the

single-atom state; copper single atoms with partially reduced clusters or nanoparticles coexisted in CAZ-15 during the reaction. As for CMZ-15 and CS-15, both the X-ray diffraction (Supplementary Fig. 6) and TEM (Supplementary Figs. 19 and 20) results indicated that almost all the copper species on the surface were reduced to larger copper particles during the reaction.

Copper loading amounts of less than 2 wt% in CAZ-x catalysts yielded CH$_3$OH as the only product because isolated Cu$_1$–O$_3$ units play a crucial role in CH$_3$OH synthesis (Fig. 2c). As the copper loading amount was increased to 4 wt%, a small amount of CO was produced because a small number of reduced copper clusters or nanoparticles were formed during the reaction (Supplementary Fig. 11), which might be active sites for the RWGS reaction. Increasing the copper content to 8 wt% also increased the proportion of CO in the products due to more copper clusters or small nanoparticles being formed. Overall, the evidence suggested that single-atom copper species with isolated Cu$_1$–O$_3$ units and copper clusters or small nanoparticles were the active sites for generating CH$_3$OH and CO, respectively. However, it was found that when the copper loading amount was further increased to 12 and 15 wt%, the CO$_2$ conversion and product distribution did not change further. Large particles of copper formed as the copper content further increased, but these do not activate CO$_2$ at low temperatures, consistent with the reaction results with CMZ-15 and CS-15 catalysts (Fig. 2a,b).

In addition, the more obvious copper bulk structure in X-ray diffraction (Fig. 4c), and the lower-temperature H_2-TPR copper reduction peak (Supplementary Fig. 10c), together indicated that more metallic copper particles were generated by reducing Cu^{2+} species over CAZ-15 during the reaction.

$Cu^{\delta+}$ species migration during the reaction. Capturing the evolution of active metal species during reactions is essential for the in-depth understanding of active sites, especially in reactions involving hydrogen. A number of studies have shown that the gases used in the pretreatment or reaction process greatly affect the structure of catalysts, including active species migration[33,34] and surface reconstruction[61,62]. A similar effect also existed in our Cu/ZrO_2 catalyst system, where the reaction gas promoted the migration of $Cu^{\delta+}$ species from bulk to the surface of the support. Time-of-flight secondary-ion mass spectrometry (TOF-SIMS) is an extremely sensitive method for analysing the dispersion of elements on a catalyst surface, and can detect the top 1–3 atomic layers of elements on such a surface (Fig. 5a,b). Figure 5 compares fresh and used catalyst: more bright red spots were detected in Fig. 5b, suggesting more copper species appeared on the surface of CAZ-1-U. Semiquantitative analysis of the copper surface (Fig. 5c) also showed that the surface of CAZ-1-U contained more copper species, indicating that these species migrate to the surface during the reaction. These results were also supported by XPS analysis (Supplementary Fig. 22): the intensity of Cu $2p$ spectra for CAZ-1-U and CAZ-15-U were much stronger than for fresh catalysts, indicating that copper species were becoming enriched on the surface of used catalysts after the reaction. Meanwhile, Cu/Zr ratios calculated by XPS further confirmed the above conclusion. The surface Cu/Zr ratios of fresh CAZ-1 and CAZ-15 samples were 0.0012 and 0.24, and the corresponding ratios for used catalysts were 0.0018 and 0.38 (Supplementary Table 5), clearly indicating that there were more active copper sites on the surface of the catalysts after the reaction. Moreover, diffuse reflectance infrared Fourier transform spectroscopy with CO absorption (DRIFT-CO) was used to verify the copper migration and supplied further important evidence. The catalysts were adsorbed to saturation in CO atmosphere before the desorption experiment was carried out with argon. The absorbed peak at $2,102\,cm^{-1}$ was assigned to linear adsorption of CO on the copper species (Supplementary Fig. 23a,b)[46,63]. For the fresh catalyst, the CO concentration decreased rapidly with the argon purge time, and the surface residual concentration was close to zero at 20 min. In comparison, the desorption rate of CO on CAZ-1-U was much slower than that on the fresh catalyst, while the obvious CO signal was still observed after 20 min of gas purging. For a more intuitive comparison, the area of the CO absorption peak was normalized to $2,102\,cm^{-1}$ to give a time-dependent surface concentration attenuation spectrum with the argon purging time (Supplementary Fig. 23c). It was concluded that the level of CO absorption on CAZ-1-U was much more than that on fresh catalyst, proving that the surface of the used catalyst contained more copper sites.

Based on the above details of the copper migration, it was inferred that a dynamic change of $Cu_1–O_3$ active sites occurred during the reaction process. EXAFS data indicated that the copper species in $Cu/a-ZrO_2$ were mainly single atoms dispersed in the fresh catalysts, and that the copper species would migrate to the surface at a certain rate under the induction of reaction gas. This explains why the reaction had a certain initial induction period (Fig. 2d and Supplementary Fig. 13). It was concluded that the unique $Cu_1–O_3$ structure in CAZ-1 was vital for CH_3OH synthesis at low temperatures. The copper sites in CAZ-1 remained copper single atoms with isolated $Cu_1–O_3$ structure after migrating to the surface due to the small amount of copper. However, more copper sites in CAZ-15 were accumulated and in situ reduced during migration in a hydrogen atmosphere process (Fig. 4c,d). Therefore,

the migration behaviour of copper species during the reaction can be divided into three types according to the catalytic activity results. When the copper content was less than 2 wt%, the migrated copper species did not accumulate during the reaction process but were still distributed in a monodispersed state, hence only CH_3OH was produced and CO_2 conversion was enhanced linearly with increasing copper loading. When the copper loading was 4–8 wt%, the copper species migrated to the surface and partially agglomerated, and the activity showed that CO_2 conversion and CO selectivity increased while CH_3OH selectivity decreased due to the formed copper clusters or small nanoparticles producing CO via the RWGS reaction. Finally, when the copper loading was higher than 8 wt%, some of the copper species aggregated to form large copper particles without CO_2 activation ability, and thus the conversion of CO_2 and the product distribution were no longer changed. A schematic diagram illustrating this is shown in Fig. 5d.

The reaction mechanism of CO_2 hydrogenation. To clarify the structure influence for absorbed species on the surface, in situ DRIFT analysis was carried out under reaction conditions. All the tests were performed at 180 °C and the assignments of all band vibration peaks are listed in Supplementary Table 7. As shown in Fig. 6a for CAZ-1, the active species were mainly first excited in HCO_3^*: the peaks located at 1,695 and $1,431\,cm^{-1}$ were assigned to ionic bicarbonate species i-HCO_3^* and the peaks at 1,631 and $1,226\,cm^{-1}$ to $v_{as}(HCO_3)$ and $v_s(HCO_3)$ of bidentate bicarbonate species b-HCO_3^* (ref. [64]), respectively. As the reaction proceeded, the HCO_3^* were slowly transformed into formate species, according to the peaks at 1,595, 1,384, 1,371, 2,736, 2,877 and $2,970\,cm^{-1}$ which were attributed to $v_{as}(OCO)$, $\delta(CH)$, $v_s(OCO)$, $\delta(CH)+v_{as}(OCO)$, $v(CH)$ and $\delta(CH)+v_s(OCO)$[21,36,65,66]. In fact, the transformation of bicarbonates to formate appears to follow the path: $HCO_3^* \rightarrow CO_2 \rightarrow HCOO^*$. The H_2 was also necessary because no evolution of HCO_3^* to $HCOO^*$ could be detected in CAZ-1 by only absorbed CO_2 (Supplementary Fig. 24). Meanwhile, vibration peaks at 1,072, 1,146, 2,827 and $2,935\,cm^{-1}$ for CH_3O^* were also detected, and assigned to $v(CO)$-terminal, $v(CO)$-bridge, $v_s(CH_3)$ and $v_{as}(CH_3)$[21,36,65]. Therefore, the process of CO_2 hydrogenation to CH_3OH in CAZ-1 followed the formate path. Furthermore, it was proved that the CH_3OH did not came from the hydrogenation process of in-situ-produced CO via the RWGS route because the reaction results showed no catalytic activity over CAZ-1 in the CO hydrogenation process under the same reaction conditions (Supplementary Table 3). For CAZ-15 catalyst, the CH_3OH signal located at $1,007\,cm^{-1}$ was detected during the in situ DRIFT test[66], which indicated the process of CH_3OH formation was strongly promoted on CAZ-15 due to the quantity of active sites for CH_3OH synthesis (Supplementary Fig. 25). In fact, the CO_2 adsorption capacity of the catalysts was not significantly changed by only increasing the loading of copper species, because CAZ-1 and CAZ-15 had similar adsorption modes and adsorption amounts for CO_2 (3.0 mmol g_{cat}^{-1} in CAZ-1, 2.9 mmol g_{cat}^{-1} in CAZ-15; Supplementary Fig. 26). It was concluded that the increase in methanol production rate was not affected by the adsorption capacity in these two catalysts, but was mainly caused by the different numbers of active sites. An increased copper loading of 15 wt% resulted in the absorption of intermediate species on the surface of CAZ-15 being much more complex than that on CAZ-1. In addition to the adsorbed bicarbonate (1,621, $1,225\,cm^{-1}$), carbonate (1,247, 1,324, 1,455, $1,505\,cm^{-1}$), formate (1,360, 1,384, 2,864, $2,974\,cm^{-1}$) and methoxy species (1,070, 1,146, 2,836, $2,921\,cm^{-1}$), carboxylate signals were also captured at 1,287 and $1,756\,cm^{-1}$ (ref. [67]). The formation of CH_3OH was accompanied by the RWGS reaction because more complex active copper sites (single-atom, cluster and particle) were provided by the reaction, leading to a decrease in CH_3OH selectivity. As for CMZ-15 with large copper nanoparticles (Supplementary Fig. 27), all the absorbed
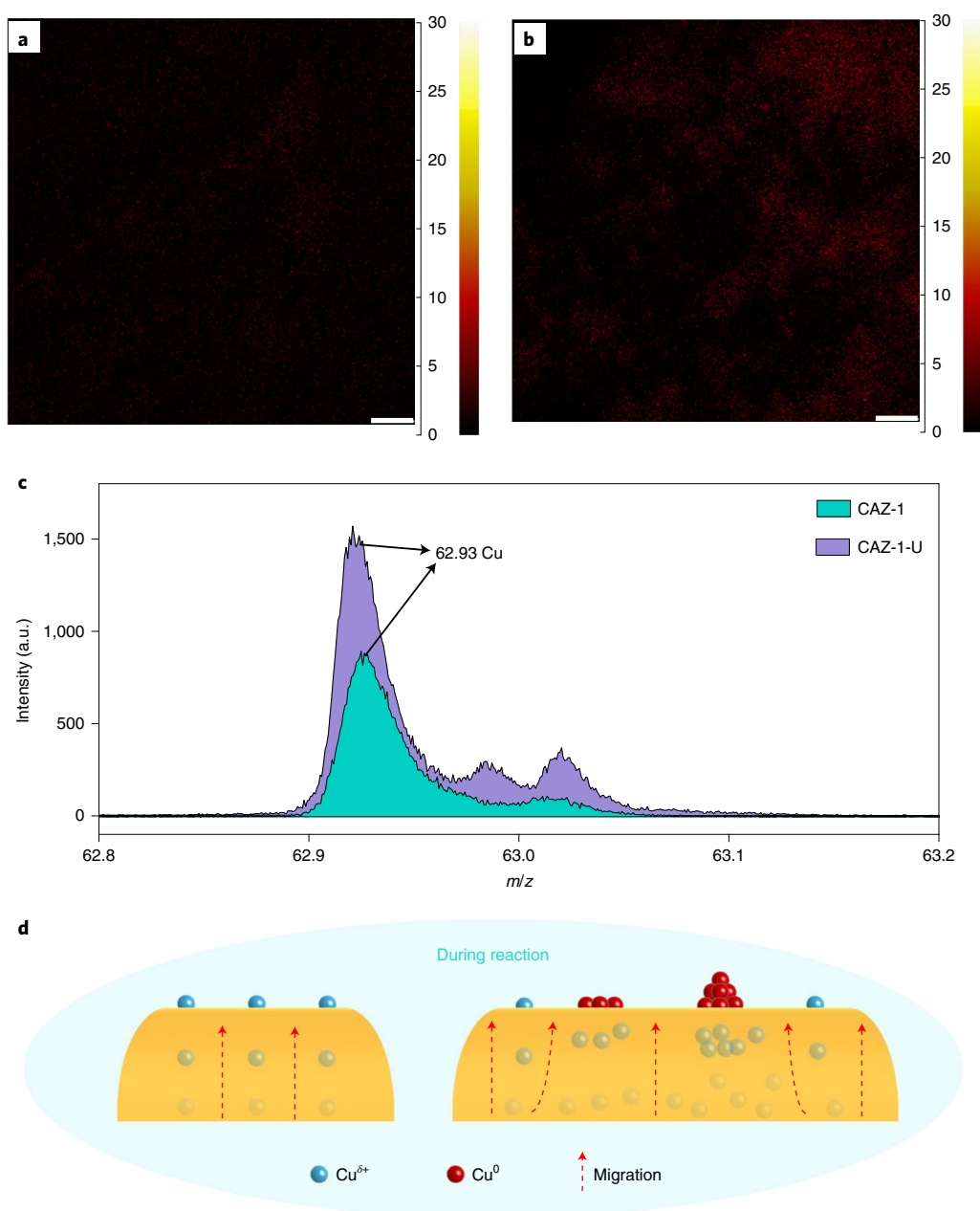
Fig. 5 | Migration of $Cu^{\delta+}$ species to the surface. a,b, TOF-SIMS images and spectra of CAZ-1 showing the copper mapping of fresh CAZ-1 (**a**) and the copper mapping of CAZ-1-U (**b**). Scale bars, 10 μm. The scale at the right of each image shows the measured intensity in counts per pixel. **c**, Semiquantitative analysis of TOF-SIMS spectra of CAZ-1 and CAZ-1-U. **d**, Schematic diagram of the migration of copper species in CAZ-1(left) and CAZ-15 (right) during the hydrogenation reaction.

species were CO_3^* or HCO_3^* but no further hydrogenation intermediates were observed, demonstrating that these large nanoparticles could not produce the further hydrogenation of carbonate at low temperature, which corresponded to the results of activity testing.

Based on the above information, intensity–time shift spectra supplied the dynamic behaviour of intermediates converting on CAZ-1 and CAZ-15 in the reaction (Fig. 6b). The peaks at 2,877 and 2,935 cm^{-1} in CAZ-1 and at 2,864 and 2,921 cm^{-1} in CAZ-15 were chosen to study the dynamic evolution of CH_3O^* and $HCOO^*$ under reaction conditions (180 °C, 3 MPa). The ratio of $HCOO^*/CH_3O^*$ increased over both CAZ-1 and CAZ-15 catalysts with longer reaction times, indicating that the transformation process of $HCOO^*$ to CH_3O^* was the rate-limiting step compared to the $HCOO^*$-generating process in the synthesis of CH_3OH from CO_2.

Furthermore, the rate of increase of $HCOO^*/CH_3O^*$ on CAZ-15 was much slower than that on CAZ-1, suggesting that the consumption of $HCOO^*$ species would be faster on the surface of CAZ-15. Because the relative rates of $HCOO^*$ formation and its further conversion to CH_3O^* were the same for each $Cu_1–O_3$ site in producing methanol over CAZ-1 and CAZ-15, the only reason to explain the different rates of increase of $HCOO^*/CH_3O^*$ over these two catalysts is that CAZ-15 contains more different types of active copper sites for $HCOO^*$ conversion reactions, such as $HCOO^* \rightarrow CO$.

The excellent selectivity to CH_3OH of CAZ-1 could be attributed to its unique $Cu_1–O_3$ catalytic centre as confirmed by density functional theory (DFT) calculations. The structure of Cu_1O_1 on amorphous ZrO_2 (Cu_1O_1/a-ZrO_2) surface was obtained by using stochastic surface walking (SSW) global optimization based on
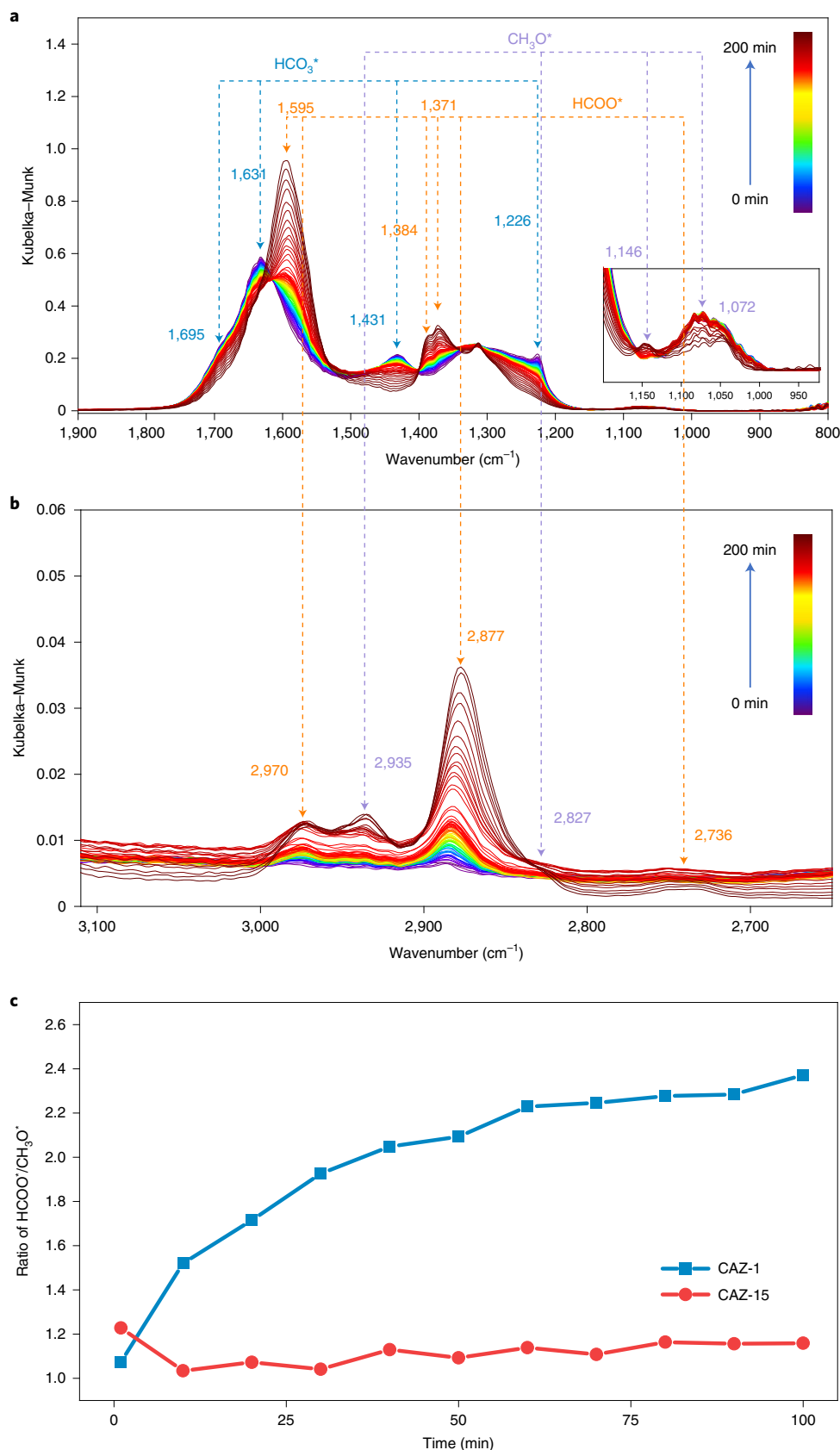
Fig. 6 | Characterization and evolution of reactive intermediates. a,b, In situ DRIFT spectroscopy of CAZ-1 for different wavenumber intervals: 800–1,900 cm^{-1} (**a**) and 2,650–3,110 cm^{-1} (**b**). Dashed lines identify the changes of peaks related to different intermediates. **c,** The ratio of HCOO* to CH$_3$O* intermediates changes as a function of time. Analysis conditions: the sample was first pretreated under an argon atmosphere at 230 °C for 60 min, then mixed gas (CO$_2$:H$_2$ = 1:3) was introduced into cell to a pressure of 3 MPa and data were recorded at 180 °C for 100 or 200 min.
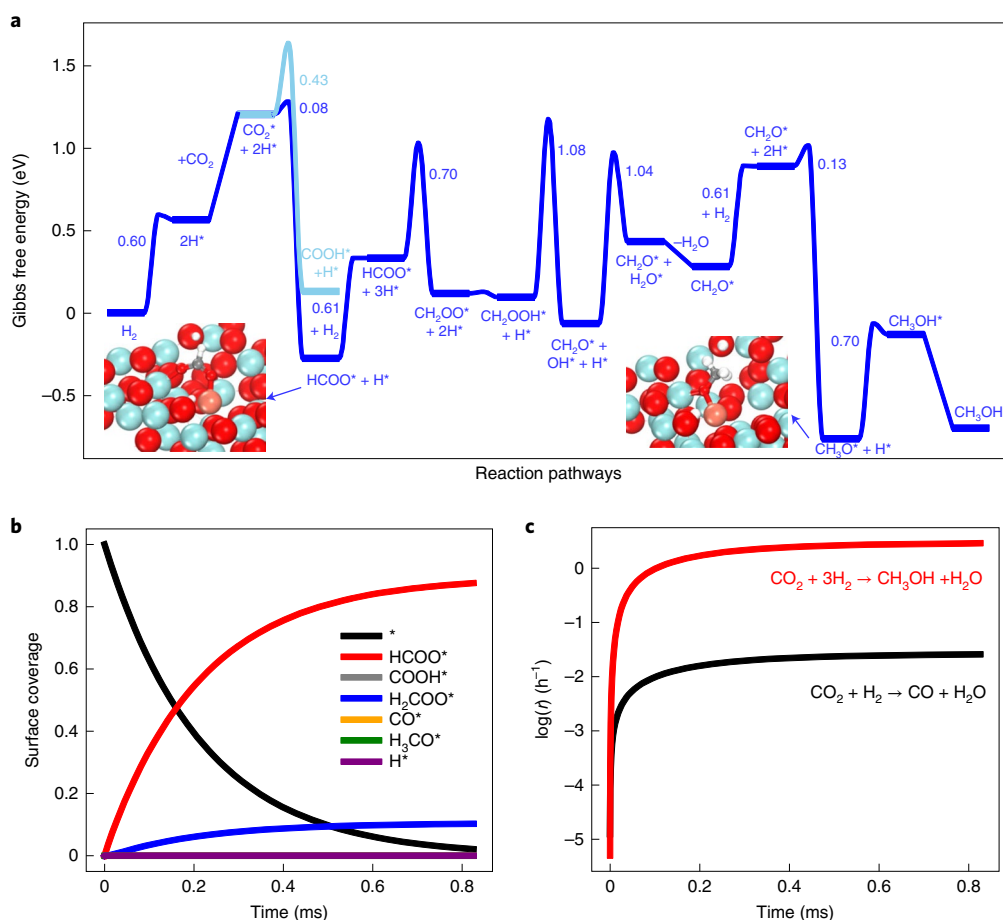
Fig. 7 | Mechanism analysis of CO_2 hydrogenation to CH_3OH/CO on isolated $Cu^{\delta+}$ ($1 < \delta < 2$) cation. a, Gibbs free-energy profile of CO_2 hydrogenation to CH_3OH/CO. **b,c**, Variation in reaction intermediate concentrations (**b**) and reaction rates (**c**) during the microkinetics simulation. The asterisk indicates the adsorption state and the reaction snapshots are shown with Cu, Zr, O, C and H in orange, cyan, red, grey and white, respectively.

global neural network potential (SSW-NN) simulation to explore the global potential energy surface of the Cu_1O_1/ZrO_2 system. The stability energy of Cu_1O_1 on a-ZrO_2 was −1.53 eV, much lower than that on ZrO_2 flat (111) and terrace (112) surfaces, which have stability energies of 1.10 and 0.17 eV that point to high thermodynamic stability (Supplementary Fig. 28a–c). The most stable structure of Cu_1O_1 on amorphous ZrO_2 showed a special Cu_1–O_3 quasiplanar configuration with Cu–O bond distances of 1.814, 1.920 and 1.921 Å (Supplementary Fig. 29), which agreed well with the EXAFS results. Moreover, the large oxygen vacancy formation energy of 3.7 eV on Cu_1O_1/a-ZrO_2 indicated the absence of O_v, further proving that the amorphous ZrO_2 surface can anchor and stabilize isolated copper atoms (Supplementary Fig. 28c). Electronic structure analysis showed that these isolated copper atoms existed in the form of Cu^{2+} cation (Supplementary Table 8), consistent with the experimental XANES results before and after the reaction. When the Cu_1O_1/a-ZrO_2 was exposed to the reaction atmosphere with reductive H_2 gas, a hydrogen atom can strongly adsorb on an oxygen atom near a copper atom with the adsorption energy of −1.76 eV. This led to the reduction of Cu^{2+} to the $Cu^{\delta+}$ ($1 < \delta < 2$) cation (Supplementary Table 8), consistent with the in situ XAS results during the reaction process (Fig. 3d). Therefore, the $Cu^{\delta+}$ cation was used as the active site to explore the mechanism of the CO_2 reduction process.

Figure 7 and Supplementary Figs. 30 and 31 show the calculated lowest-energy pathway for CO_2 hydrogenation, which involves HCOO*, H_2COO* and CH_3O* key intermediates. The reaction

started with the dissociative adsorption of an H_2 molecule on a Cu–O pair to form Cu–H and OH groups (Supplementary Fig. 32), which was endothermic at 0.57 eV. The dissociation energy barrier of H_2 is 0.61 eV. A CO_2 molecule was adsorbed physically near the Cu–H group, resulting in a free-energy change of 0.64 eV. While there were two possible channels for CO_2 hydrogenation, that is, to HCOO* or to COOH*, our calculations showed that the formation of the COOH* group had a high barrier of 0.43 eV, but the formation of HCOO* was nearly barrierless (0.08 eV). Thermodynamically, the COOH* group was also 0.39 eV less stable than the HCOO* group. The formed HCOO* adopted a bidentate configuration with two oxygen ends linking with the zirconium and copper atoms at distances of 2.20 and 1.85 Å, respectively. This indicated that the HCOO* pathway was the only viable route for CO_2 hydrogenation.

After HCOO* formation, a second H_2 molecule dissociated on the copper and the neighbouring two-coordinated surface oxygen with an endothermic energy of 0.61 eV. The C atom of the HCOO* group could then be hydrogenated to CH_2OO* group with a barrier of 0.70 eV and a reaction energy of 0.22 eV. After that, CH_2OO* could easily pick up the neighbouring hydrogen atom to form CH_2OOH* with a barrier of only 0.01 eV. The CH_2OOH* could further break the C–O bond to form CH_2O* and hydroxyl groups by overcoming a barrier of 1.08 eV. The generated hydroxyl groups could react with the neighbouring hydrogen atom to form a water molecule with a reaction barrier of 1.04 eV and a reaction energy of 0.50 eV. The water molecule could desorb readily (exothermic by 0.15 eV). CH_2O* could stepwise react with neighbouring
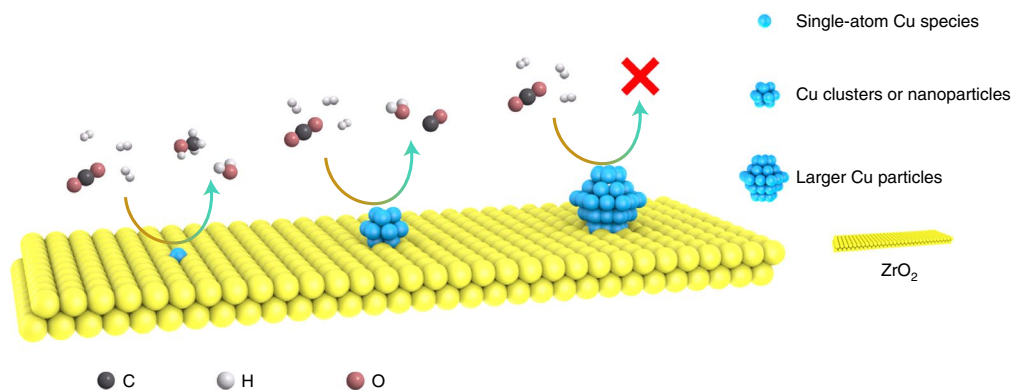
Fig. 8 | Schematic diagram for CO₂ hydrogenation reaction on different types of copper species. The physical model correlates the particle diameter and the CO₂ hydrogenation reaction pathway at low temperature: CO₂/H₂ can only produce methanol on single-atom copper species; on copper clusters or nanoparticles, only CO generation can be promoted; larger copper particles have almost no catalytic activity to CO₂/H₂ mixed gas. Reaction conditions: 0.5 g sample, 3 MPa, 180 °C, CO₂:H₂ = 1:3, 10 ml min⁻¹.

hydrogen atoms to form CH₃O* and CH₃OH*. The reaction barriers for these two hydrogenation steps were 0.13 and 0.70 eV with the reaction energies being −1.66 and 0.63 eV, respectively. The desorption of CH₃OH would further release 0.57 eV energy.

Having established the overall reaction profiles, we can now determine the reaction rate of CO₂ hydrogenation on an isolated $Cu^{\delta+}$ cation site based on microkinetics simulation. Our microkinetics numerical simulation results are shown in Fig. 7b. At the steady state, the dominant reaction intermediates on the surface were HCOO* species, the concentration of which increased from 0 to 0.8 with increasing time. This proved that the consumption of HCOO* species was the rate-determining step, a finding that is consistent with the in-situ DRIFT spectroscopy. At 180 °C, the calculated TOF for CO₂ hydrogenation to CH₃OH on an isolated $Cu^{\delta+}$ cation was around 2.89 h⁻¹, which was about two orders of magnitude larger than the CO₂ hydrogenation to CO (0.03 h⁻¹), as illustrated in Fig. 7c, and the selectivity of CO₂ hydrogenation to methanol was near 100%. The theoretical TOF for CO₂ hydrogenation to methanol was quite close to the experimental TOF value (1.37 h⁻¹).

Based on the above results, we can establish a reaction model for CO₂ hydrogenation over the CAZ-*x* series catalysts, as shown in Fig. 8. When the copper species is distributed in a single-atom level with uniform Cu₁−O₃ catalytic centres on the surface of ZrO₂, CO₂ is converted to methanol with 100% selectivity. When the copper species exists in the form of clusters or small nanoparticles, CO₂ can only produce unwanted CO. As the copper species is in larger particles, CO₂ is hard to activate and there is almost no catalytic activity. Under typical catalytic conditions, the Cu₁−O₃ sites in copper single atoms and the copper clusters/small nanoparticles in combination contribute to methanol and CO synthesis from CO₂ hydrogenation, while the larger copper particles are not active sites for CO₂ hydrogenation.

Conclusions

This work reveals the strong dependence of CO₂ hydrogenation activity and selectivity on the nature of surface copper species for Cu/ZrO₂ catalysts. The undercoordinated cationic Cu₁−O₃ species accumulate dynamically on the catalyst surface, forming stable active sites during the catalysis process, and achieving high selectivity to CH₃OH (100%) in CO₂ hydrogenation at 180 °C. The copper single-atom catalyst can dissociate hydrogen readily with the help of nearby oxygen atoms and activate CO₂ to generate HCOO*, a key intermediate in CH₃OH synthesis. The HCOO* pathway is the only viable route for CO₂ hydrogenation on the isolated Cu₁−O₃ active sites. In contrast, small copper clusters and/or nanoparticles are

active sites for CO formation via the RWGS route, while large copper particles barely activate CO₂ at low temperatures. The characteristic geometry and unique activity revealed in the copper single-atom catalyst provide a deep understanding of copper-catalysed CO₂ hydrogenation, and will guide future applications of single-atom catalysts in thermal catalytic CO₂ transformations.

Methods

Synthesis of CAZ-1. CAZ-1 was synthesized by a co-precipitation method using Na₂CO₃ as precipitant. First, Cu(NO₃)₂·3H₂O (Sigma-Aldrich, 98–103%) and Zr(NO₃)₄·5H₂O (Macklin, AR) precursors were weighed according to the metal loading and dissolved together into 100 ml deionized water to make a 0.03 M solution (solution A). An appropriate amount of Na₂CO₃ was weighed and dissolved in 100 ml deionized water to make a 0.06 M solution (solution B). After dissolution was complete, a peristaltic pump was used to slowly drip the two solutions A and B into another beaker containing 100 ml of deionized water at a rate of 0.3 ml min⁻¹. Throughout the dropping process, the mixture was stirred at 350 rpm while heating at 80 °C. Once the dropping was complete, stirring was stopped and the flocculent precipitate that had formed was aged at 80 °C for 2 h. After ageing, it was cooled to room temperature and washed with deionized water to pH 7, followed by drying in an oven at 80 °C overnight. Finally, the blue solid sample was ground into powder and calcined in a muffle furnace by heating at 2 °C min⁻¹ to 350 °C over 5 h.

Catalyst characterization. The actual loading of copper in different catalysts was determined by ICP-OES performed on an iCAP 7000 (Thermo Fisher). The test method was as follows: 10 mg of sample was dissolved in a mixed solution (2 ml HNO₃+6 ml HCl+2 ml HF) overnight, then added to a 50 ml volumetric flask and diluted to the scale line. Four internal copper concentration standard solutions (1, 10, 50, 100 ppm) were analysed and used to create a standard curve ($R^2 > 0.9999$) before testing all samples. X-ray diffraction measurements were performed on a Rigaku X-ray diffractometer equipped with graphite-monochromatized Cu Kα radiation (scan angle, 10°–90°; scan speed, 2° min⁻¹; voltage, 40 kV; current, 40 mA). The Raman spectroscopy data were collected on a Thermo Fisher DXR2xi with a 532 nm light source. In situ X-ray diffraction experiments were carried out on a Rigaku Ultima 4 X-ray diffractometer with Cu Kα radiation (40 kV, 40 mA) in the temperature range of 10°–80 °C with a scanning step length of 0.33 under a hydrogen atmosphere (30 ml min⁻¹). The curves were recorded at 30, 180, 230, 300 and 350 °C. The morphology and elemental mapping of catalysts were measured on a JEM ARM200F thermal-field emission microscope with a probe spherical aberration (Cs) corrector working at 200 kV, and by TEM (FEI Talos F200S G2) at 200 kV. The H₂-TPR curves of samples were collected with an AutoChem II 2920 chemisorption analyser (Micromeritics) equipped with a thermal conductivity detector (TCD). Helium at 30 ml min⁻¹ was used to pretreat the samples at 250 °C for 2 h to remove moisture from the surface. Then 10% H₂/He was passed into the reactor, with the temperature increasing at 10 °C min⁻¹ to 700 °C, and data were recorded every 0.5 min. H₂-TPD curves of samples were also collected on an AutoChem II 2920 chemisorption analyser (Micromeritics). The samples were first pretreated at 300 °C at a heating rate of 10 °C min⁻¹ in helium for 30 min, and then cooled to room temperature and further saturated by 10% H₂/Ar for 30 min. After purging the physically adsorbed hydrogen on the surface with helium at 50 °C for 1 h, the temperature was slowly increased to 750 °C and the thermal

conductivity detector signal recorded at the same time. CO_2-TPD measurements were performed in the same way as for H_2-TPD except that 5% CO_2 was used as the adsorption gas.

XPS and AES data were collected on an ESCALAB 250 photoelectron spectroscope (Thermo Fisher Scientific) equipped with monochromatic Al Kα radiation (200 W, $E = 1,486.6$ eV). The binding energy of all samples was calibrated to the C $1s$ peak of environmental carbon at 284.8 eV.

The ex situ and in situ XAS experiments were performed at beamline BL14W1 of the Shanghai Synchrotron Radiation Facility (SSRF) in fluorescence mode with a Si(111) monochromator. A Lytle detector and a silicon solid detector were used to collect ex situ and in situ XAS data, respectively. At the same time, a 6 μm nickel filter was used to filter the signal. A copper foil was taken as a reference sample and measured for energy-calibration purposes ($E_0 = 8,979$ eV). The first maximum point of the first-order derivative of the XANES was defined as E_0. For ex situ experiments, Cu K-edge spectra were collected at room temperature (25 °C). The CAZ-1, CAZ-1-U, CAZ-15 and CMZ-15 samples were pressed into pellets without any dilution. The in situ testing for CAZ-1 catalyst was performed by using a reactor with a beryllium window. Multiple repeated scans (~20 min for each scan) were applied to achieve high data quality. Multiple data scans were collected and merged to improve the signal-to-noise ratio. A K-type thermocouple was placed in contact with the catalyst bed to control the temperature, and the flow rate of the gas was controlled by multiple flow controllers. CAZ-1 sample was first pressed into a 1.5 cm disc, then placed in a cell for pretreatment at 230 °C under an argon gas flow (30 ml min⁻¹) for 2 h. The temperature was then lowered to 180 °C and the gas changed to CO_2/H_2 (25/75, 10 ml min⁻¹). After the pressure was stabilized at 1 MPa, the continuous spectrum was collected. EXAFS data processing (including calibration, merge, and analysis) was done with Athena/Artemis software packages[68], based on FEFF6. Bond length (R), Debye–Waller factor (σ^2), amplitude factor (S_0^2) and energy shift (ΔE_0) were used to optimize the fitting results. The WT was performed with the HAMA Fortran package (http://www.esrf.eu/UsersAndScience/Experiments/CRG/BM20/Software/Wavelets/HAMA). In a typical WT analysis, $k_{weight} = 2$, and the Morlet function was used, with $\kappa = 10$, $\sigma = 1$.

DRIFT-CO chemisorption measurements were carried on a Nicolet iS50 spectrometer (Thermo Fisher Scientific) with a mercury–cadmium–telluride detector and a Harrick reaction cell. The sample was first treated in an argon atmosphere (30 ml min⁻¹) at 300 °C for 30 min, then cooled to 30 °C for background collection. After that, 10% CO/Ar was passed through the sample until the adsorption was saturated, then the 10% CO/Ar was cut off and the desorption spectra recorded as 32 scans at a resolution of 4 cm⁻¹ under an argon purge. In situ DRIFT experiments at high pressure (3 MPa) were measured on a Fourier transform infrared spectrometer (Bruker Vertex 70) with a mercury–cadmium–telluride detector and a Harrick reaction cell. The samples were first pretreated with helium at 230 °C or hydrogen at 250 °C for 60 min, then cooled to 150 °C and treated with $CO_2/H_2/Ar$ (24/72/4) or CO_2 alone. After the pressure reached 3 MPa the background was collected. Finally, the temperature was raised to 180 °C and the spectra recorded over the absorption time.

TOF-SIMS experiments were tested on a PHI nano TOF II with Bi_3^+ as the ion species. The energy, ion current, raster size, mass range, mode and analysis time for each test were 30 keV, 2 nA, 100 μm × 100 μm, 0–1,850 μg/L, high mass resolution mode and 5 min, respectively.

The H_2–D_2 exchange experiments were carried out in a flow reactor at 180 °C, and the formation rate of the HD product was measured by the mass signal intensity (ionic current). First, 0.1 g sample was pretreated for 1 h in different (30 ml min⁻¹) atmospheres (pure a-ZrO_2, CAZ-1-U, CAZ-15-U and pure Q50 were pretreated at 230 °C with argon, CMZ-15 was pretreated at 250 °C with hydrogen), followed by passing a mixture of D_2 and H_2 (10 ml min⁻¹) through the sample. The reaction products H_2, D_2 and HD were analysed by mass spectrometry (OmniStar). The mass-to-charge ratios using H_2, D_2 and HD are 2, 4 and 3, respectively.

Catalytic evaluation. The catalytic performance of all catalysts was tested on a high-pressure, continuous-flow, fixed-bed reactor built by Xiamen Better Works Engineering. We mixed 500 mg of CAZ-x catalysts (40–60 mesh) with 2 g of quartz sand (40–60 mesh) and pretreated this mixture in an argon atmosphere at 230 °C (CAZ-1-r was reduced by H_2 at 370 °C) in a flow of 30 ml min⁻¹ for 10 h. CMZ-15 and CS-15 were pretreated with hydrogen at 250 °C in a flow of 30 ml min⁻¹ for 10 h. The temperature was then cooled to 180 °C, and $CO_2/H_2/Ar$ (24/72/4, 3 MPa) was introduced. After the pressure and temperature stabilized, the gas flow was changed to 10 ml min⁻¹ and a Shimadzu chromatograph equipped with a flame ionization detector and a thermal conductivity detector was used to analyse products online every 30 min. The catalytic performance of catalysts was evaluated in terms of CO_2 conversion, product selectivity, TOF and space-time yield (STY). The computational formulas were as follows:

$$CO_2 \text{ conversion}, C_{CO_2} (\%) = \frac{X_{CO_2,in} - X_{CO_2,out}}{X_{CO_2,in}} \times 100\% \quad (1)$$

$$\text{Product } (i) \text{ selectivity}, Sel_i\% = \frac{R_i \times f_{i,m}}{\sum_i R_i \times f_{i,m}} \times 100\% \quad (2)$$

$$\text{TOF of methanol formation, } TOF_{CH_3OH} (h^{-1}) = \frac{F_{CO_2,in} \times C_{CO_2} \times Sel_{CH_3OH} \times M_{Cu}}{W_{cat} \times L_{Cu}} \quad (3)$$

$$\text{STY of methanol, } STY_{CH_3OH} \left(mmol_{CH_3OH} \, g_{cat}^{-1} \, h^{-1} \right) = \frac{F_{CO_2,in} \times C_{CO_2} \times Sel_{CH_3OH} \times 1,000}{W_{cat}} \quad (4)$$

where $X_{CO_2,in}$ and $X_{CO_2,out}$ are the mole fractions of CO_2 in pristine and exit mixed gas, respectively; R_i is the area ratio of products in the chromatogram, $f_{i,m}$ is the correction for mass; $F_{CO_2,in}$ (mol h⁻¹) is the molar flow rate of CO_2 in pristine mixed gas; M_{Cu} is the molecular weight of copper, 63.546 g mol⁻¹; and W_{cat} (g) and L_{Cu} (%) are the catalyst weight and the actual loading of copper, respectively.

DFT calculations. The reaction profiles were calculated using plane-wave DFT calculations as implemented in VASP[69], where electron–ion interaction was represented by the projector-augmented wave pseudopotential[70,71]. The exchange functional utilized was the spin-polarized GGA-PBE[72] and the kinetic energy cut-off was set as 450 eV. The first Brillion zone k-point sampling utilizes only the gamma-point since the supercell was rather large, which was shown to provide converged energetics. The energy and force criterion for convergence of the electron density and structure optimization were set at 10^{-5} eV and 0.05 eV Å⁻¹, respectively.

SSW-NN simulation. The active site structure was resolved by the machine-learning-based fast global potential energy surface (PES) exploration using the SSW method as implemented in LASP code[73]. The PES of the catalyst system (containing elements Cu, Zr, O and H) was described by the global neural network (G-NN) potential, which was generated by iteratively self-learning the global PES dataset from SSW exploration. In the past few years, the SSW-NN method has been successfully applied in solving the structures of complex systems, including oxide[13,74,75], zeolite[74] and molecule crystals[76]. The procedure for SSW-NN simulation is briefly summarized below.

First, the global dataset was built iteratively during the self-learning of the G-NN potential. These PES data came initially from the DFT-based SSW simulation and were then amended by G-NN-based SSW PES exploration. To cover all the likely compositions of the four-element Cu–Zr–O–H systems, SSW simulations were performed starting from different types of structures (including bulk, layer and cluster), compositions and atom numbers per supercell. Overall, these SSW simulations generated more than 10^7 structural configurations on the PES and a fraction of these were selected as the dataset to be computed by high-accuracy DFT calculations. The final dataset of the Cu–Zr–O–H G-NN potential contains 60,271 structures, as detailed in Supplementary Table 9.

Second, a final G-NN potential was trained on the global dataset using the method introduced in our previous work[77,78]. To achieve a high accuracy for PES, we adopted a large set of power-type structure descriptors, which contained 324 descriptors for every element, including 148 two-body, 170 three-body and 6 four-body descriptors, and compatibly, the neural network had two hidden layers (324-50-50-1 net) each with 50 neurons and one output layer with one neuron, equivalent to 75,000 network parameters in total. Minimum–maximum scaling was utilized to normalize the training data sets. Hyperbolic tangent activation functions were used for the hidden layers, while a linear transformation was applied to the output layer of all networks. The limited-memory Broyden–Fletcher–Goldfarb–Shanno method was used to minimize the loss function to match DFT energy, force and stress. The final energy and force criterions of the r.m.s. errors of the G-NN potential were 6.0 meV per atom and 0.151 eV Å⁻¹, respectively. The NN potential of CuZrOH.pot can be found at www.lasphub.com/supportings/CuZrOH.pot.

Finally, SSW-NN global optimization was utilized to obtain a reasonable model of Cu_{SAC} on amorphous ZrO_2 by exhaustively searching the phase space of Cu_1O_1/ZrO_2. The model was built as follows:

1. From the most stable monoclinic ZrO_2 bulk structure, the most stable (−111) surface in a p (4×4) supercell was cleaved that contains three ZrO_2 layers with 144 atoms (48 ZrO_2 formula units).
2. To create defects, three ZrO_2 formula units (nine atoms) were artificially removed from the m-ZrO_2 (−111) surface, and utilized to represent the locally amorphous structure (Supplementary Fig. 33).
3. One CuO formula unit (two atoms) was randomly added at the ZrO_2 defect sites.
4. Starting from the Cu_1O_1/ZrO_2 model, more than 10,000 minima were explored by SSW-NN simulation. From that, the most stable structure of Cu_1O_1 on amorphous ZrO_2 was obtained, which featured a special Cu_1–O_3 quasiplanar configuration decorated at the ZrO_2 defect sites. This structure had Cu–O bond distances of 1.814, 1.920 and 1.921 Å (Supplementary Fig. 29), which were very consistent with the EXAFS results. The stable structures were then verified by DFT calculations and then adopted for further computing the CO_2 hydrogenation pathway.

Data availability
Data presented in the main figures of the manuscript and Supplementary Information are publicly available through the Zenodo repository (https://zenodo.org/deposit/6874758); all other relevant raw data are available from the corresponding authors upon reasonable request. Source data are provided with this paper.

Code availability

References

1. Li, J. et al. Integrated tuneable synthesis of liquid fuels via Fischer–Tropsch technology. *Nat. Catal.* **1**, 787–793 (2018).
2. Jenkinson, D. S., Adams, D. E. & Wild, A. Model estimates of CO_2 emissions from soil in response to global warming. *Nature* **351**, 304–306 (1991).
3. Kang, X. et al. Highly efficient electrochemical reduction of CO_2 to CH_4 in an ionic liquid using a metal–organic framework cathode. *Chem. Sci.* **7**, 266–273 (2016).
4. Zhong, J. et al. State of the art and perspectives in heterogeneous catalysis of CO_2 hydrogenation to methanol. *Chem. Soc. Rev.* **49**, 1385–1413 (2020).
5. Yao, B. et al. Transforming carbon dioxide into jet fuel using an organic combustion-synthesized Fe–Mn–K catalyst. *Nat. Commun.* **11**, 6395 (2020).
6. Hu, J. et al. Sulfur vacancy-rich MoS_2 as a catalyst for the hydrogenation of CO_2 to methanol. *Nat. Catal.* **4**, 242–250 (2021).
7. Tan, L. et al. Development of soluble UiO-66 to improve photocatalytic CO_2 reduction. *Catal. Today* https://doi.org/10.1016/j.cattod.2022.05.001 (2022).
8. Ferri, P. et al. Chemical and structural parameter connecting cavity architecture, confined hydrocarbon pool species, and MTO product selectivity in small-pore cage-based zeolites. *ACS Catal.* **9**, 11542–11551 (2019).
9. Ilias, S. & Bhan, A. Mechanism of the catalytic conversion of methanol to hydrocarbons. *ACS Catal.* **3**, 18–31 (2013).
10. Tan, L. et al. Bifunctional capsule catalyst of Al_2O_3@Cu with strengthened dehydration reaction field for direct synthesis of dimethyl ether from syngas. *Ind. Eng. Chem. Res.* **58**, 22905–22911 (2019).
11. Tan, L. et al. Design of a core–shell catalyst: an effective strategy for suppressing side reactions in syngas for direct selective conversion to light olefins. *Chem. Sci.* **11**, 4097–4105 (2020).
12. Tan, L. et al. Direct CO_2 hydrogenation to light olefins by suppressing CO by-product formation. *Fuel Process. Technol.* **196**, 106174 (2019).
13. Ma, S., Huang, S.-D. & Liu, Z.-P. Dynamic coordination of cations and catalytic selectivity on zinc–chromium oxide alloys during syngas conversion. *Nat. Catal.* **2**, 671–677 (2019).
14. Behrens, M. et al. The active site of methanol synthesis over $Cu/ZnO/Al_2O_3$ industrial catalysts. *Science* **336**, 893–897 (2012).
15. Beck, A. et al. Following the structure of copper–zinc–alumina across the pressure gap in carbon dioxide hydrogenation. *Nat. Catal.* **4**, 488–497 (2021).
16. Shi, Z. et al. CO_2 hydrogenation to methanol over Cu–In intermetallic catalysts: effect of reduction temperature. *J. Catal.* **379**, 78–89 (2019).
17. Li, K. & Chen, J. G. CO_2 hydrogenation to methanol over ZrO_2-containing catalysts: insights into ZrO_2 induced synergy. *ACS Catal.* **9**, 7840–7861 (2019).
18. Samson, K. et al. Influence of ZrO_2 structure and copper electronic state on activity of Cu/ZrO_2 catalysts in methanol synthesis from CO_2. *ACS Catal.* **4**, 3730–3741 (2014).
19. Wu, C. et al. Inverse ZrO_2/Cu as a highly efficient methanol synthesis catalyst from CO_2 hydrogenation. *Nat. Commun.* **11**, 5767 (2020).
20. Bahruji, H. et al. Pd/ZnO catalysts for direct CO_2 hydrogenation to methanol. *J. Catal.* **343**, 133–146 (2016).
21. Wang, J. et al. A highly selective and stable $ZnO–ZrO_2$ solid solution catalyst for CO_2 hydrogenation to methanol. *Sci. Adv.* **3**, e1701290 (2017).
22. Martin, O. et al. Indium oxide as a superior catalyst for methanol synthesis by CO_2 hydrogenation. *Angew. Chem. Int. Ed.* **55**, 6261–6265 (2016).
23. Wang, J. et al. High-performance $MaZrO_x$ (Ma = Cd, Ga) solid-solution catalysts for CO_2 hydrogenation to methanol. *ACS Catal.* **9**, 10253–10259 (2019).
24. Sharafutdinov, I. et al. Intermetallic compounds of Ni and Ga as catalysts for the synthesis of methanol. *J. Catal.* **320**, 77–88 (2014).
25. Kong, H., Li, H.-Y., Lin, G.-D. & Zhang, H.-B. Pd-decorated CNT-promoted $Pd–Ga_2O_3$ catalyst for hydrogenation of CO_2 to methanol. *Catal. Lett.* **141**, 886 (2011).
26. Bai, S., Shao, Q., Feng, Y., Bu, L. & Huang, X. Highly efficient carbon dioxide hydrogenation to methanol catalyzed by zigzag platinum–cobalt nanowires. *Small* **13**, 1604311 (2017).
27. Graciani, J. et al. Highly active copper–ceria and copper–ceria–titania catalysts for methanol synthesis from CO_2. *Science* **345**, 546–550 (2014).
28. Yu, J. et al. Stabilizing Cu^+ in Cu/SiO_2 catalysts with a shattuckite-like structure boosts CO_2 hydrogenation into methanol. *ACS Catal.* **10**, 14694–14706 (2020).
29. Yang, H. et al. A highly stable copper-based catalyst for clarifying the catalytic roles of Cu^0 and Cu^+ species in methanol dehydrogenation. *Angew. Chem. Int. Ed.* **57**, 1836–1840 (2018).
30. Karelovic, A. & Ruiz, P. The role of copper particle size in low pressure methanol synthesis via CO_2 hydrogenation over Cu/ZnO catalysts. *Catal. Sci. Technol.* **5**, 869–881 (2015).
31. Rong, W. et al. Size-dependent activity and selectivity of atomic-level copper nanoclusters during CO/CO_2 electroreduction. *Angew. Chem. Int. Ed.* **60**, 466–472 (2021).
32. Zhu, Y. et al. Copper–zirconia interfaces in UiO-66 enable selective catalytic hydrogenation of CO_2 to methanol. *Nat. Commun.* **11**, 5849 (2020).
33. Zhou, H. et al. Engineering the Cu/Mo_2CT_x (MXene) interface to drive CO_2 hydrogenation to methanol. *Nat. Catal.* **4**, 860–871 (2021).
34. Tada, S. et al. Design of interfacial sites between Cu and amorphous ZrO_2 dedicated to CO_2-to-methanol hydrogenation. *ACS Catal.* **8**, 7809–7819 (2018).
35. Tada, S. et al. Cu species incorporated into amorphous ZrO_2 with high activity and selectivity in CO_2-to-methanol hydrogenation. *J. Phys. Chem. C.* **122**, 5430–5442 (2018).
36. Ma, Y. et al. Reactivity of a zirconia–copper inverse catalyst for CO_2 hydrogenation. *J. Phys. Chem. C.* **124**, 22158–22172 (2020).
37. Qiao, B. et al. Single-atom catalysis of CO oxidation using Pt_1/FeO_x. *Nat. Chem.* **3**, 634–641 (2011).
38. Nguyen, L. et al. Ir_1Zn_n bimetallic site for efficient production of hydrogen from methanol. *ACS Sustain. Chem. Eng.* **7**, 18793–18800 (2019).
39. Tang, Y. et al. Synergy of single-atom Ni_1 and Ru_1 sites on CeO_2 for dry reforming of CH_4. *J. Am. Chem. Soc.* **141**, 7283–7293 (2019).
40. Li, H. et al. Synergetic interaction between neighbouring platinum monomers in CO_2 hydrogenation. *Nat. Nanotechnol.* **13**, 411–417 (2018).
41. Ye, X. et al. Highly selective hydrogenation of CO_2 to ethanol via designed bifunctional $Ir_1–In_2O_3$ single-atom catalyst. *J. Am. Chem. Soc.* **142**, 19001–19005 (2020).
42. Han, Z., Tang, C., Wang, J., Li, L. & Li, C. Atomically dispersed Pt_n^+ species as highly active sites in Pt/In_2O_3 catalysts for methanol synthesis from CO_2 hydrogenation. *J. Catal.* **394**, 236–244 (2021).
43. Witoon, T., Chalorngtham, J., Dumrongbunditkul, P., Chareonpanich, M. & Limtrakul, J. CO_2 hydrogenation to methanol over Cu/ZrO_2 catalysts: effects of zirconia phases. *Chem. Eng. J.* **293**, 327–336 (2016).
44. Chen, C. et al. The significant role of oxygen vacancy in Cu/ZrO_2 catalyst for enhancing water–gas shift performance. *Int. J. Hydrog. Energy* **39**, 317–324 (2014).
45. Ikuno, T. et al. Methane oxidation to methanol catalyzed by Cu-oxo clusters stabilized in NU-1000 metal–organic framework. *J. Am. Chem. Soc.* **139**, 10294–10301 (2017).
46. Wang, L.-C. et al. Structural evolution and catalytic properties of nanostructured Cu/ZrO_2 catalysts prepared by oxalate gel-coprecipitation technique. *J. Phys. Chem. C.* **111**, 16549–16557 (2007).
47. Velu, S., Suzuki, K., Gopinath, C. S., Yoshida, H. & Hattori, T. XPS, XANES and EXAFS investigations of $CuO/ZnO/Al_2O_3/ZrO_2$ mixed oxide catalysts. *Phys. Chem. Chem. Phys.* **4**, 1990–1999 (2002).
48. Qian, J. et al. Exploration of $CeO_2–CuO$ quantum dots in situ grown on graphene under hypha assistance for highly efficient solar-driven hydrogen production. *Inorg. Chem.* **57**, 14532–14541 (2018).
49. Yuan, L. et al. Dynamic evolution of atomically dispersed Cu species for CO_2 photoreduction to solar fuels. *ACS Catal.* **9**, 4824–4833 (2019).
50. Qiu, X. et al. Hybrid Cu_xO/TiO_2 nanocomposites as risk-reduction materials in indoor environments. *ACS Nano* **6**, 1609–1618 (2012).
51. Yang, J. et al. Dynamic behavior of single-atom catalysts in electrocatalysis: identification of $Cu-N_3$ as an active site for the oxygen reduction reaction. *J. Am. Chem. Soc.* **143**, 14530–14539 (2021).
52. Nosaka, Y., Takahashi, S., Sakamoto, H. & Nosaka, A. Y. Reaction mechanism of Cu(II)-grafted visible-light responsive TiO_2 and WO_3 photocatalysts studied by means of ESR spectroscopy and chemiluminescence photometry. *J. Phys. Chem. C* **115**, 21283–21290 (2011).
53. Chusuei, C. C., Brookshier, M. A. & Goodman, D. W. Correlation of relative X-ray photoelectron spectroscopy shake-up intensity with CuO particle size. *Langmuir* **15**, 2806–2808 (1999).
54. Sato, A. G. et al. Effect of the ZrO_2 phase on the structure and behavior of supported Cu catalysts for ethanol conversion. *J. Catal.* **307**, 1–17 (2013).
55. Lamberti, C. et al. XAFS, IR, and UV–vis study of the CuI environment in CuI–ZSM-5. *J. Phys. Chem. B* **101**, 344–360 (1997).
56. Zhang, Z. et al. Transfer hydrogenation of fatty acids on Cu/ZrO_2: demystifying the role of carrier structure and metal–support interface. *ACS Catal.* **10**, 9098–9108 (2020).
57. Cui, G. et al. ZrO_2-x modified Cu nanocatalysts with synergistic catalysis towards carbon–oxygen bond hydrogenation. *Appl. Catal. B* **280**, 119406 (2021).
58. Gao, J. et al. Cu_2In nanoalloy enhanced performance of Cu/ZrO_2 catalysts for the CO_2 hydrogenation to methanol. *Ind. Eng. Chem. Res.* **59**, 12331–12337 (2020).
59. Zhang, Z. et al. The most active Cu facet for low-temperature water gas shift reaction. *Nat. Commun.* **8**, 488 (2017).

60. Ladera, R. et al. Catalytic valorization of CO_2 via methanol synthesis with Ga-promoted Cu–ZnO–ZrO$_2$ catalysts. *Appl. Catal. B* **142-143**, 241–248 (2013).

61. Zhang, X. et al. Reaction-driven surface reconstruction of ZnAl$_2$O$_4$ boosts the methanol selectivity in CO_2 catalytic hydrogenation. *Appl. Catal. B* **284**, 119700 (2021).

62. Yan, G. et al. Reaction product-driven restructuring and assisted stabilization of a highly dispersed Rh-on-ceria catalyst. *Nat. Catal.* **5**, 119–127 (2022).

63. Dandekar, A. & Vannice, M. A. Determination of the dispersion and surface oxidation states of supported Cu catalysts. *J. Catal.* **178**, 621–639 (1998).

64. Pokrovski, K., Jung, K. T. & Bell, A. T. Investigation of CO and CO_2 adsorption on tetragonal and monoclinic zirconia. *Langmuir* **17**, 4297–4303 (2001).

65. Yang, C. et al. Strong electronic oxide–support interaction over In$_2$O$_3$/ZrO$_2$ for highly selective CO_2 hydrogenation to methanol. *J. Am. Chem. Soc.* **142**, 19523–19531 (2020).

66. Wang, Y. et al. Strong evidence of the role of H$_2$O in affecting methanol selectivity from CO_2 hydrogenation over Cu–ZnO–ZrO$_2$. *Chem* **6**, 419–430 (2020).

67. Li, H. et al. CO_2 activation on ultrathin ZrO$_2$ film by H$_2$O co-adsorption: in situ NAP-XPS and IRAS studies. *Surf. Sci.* **679**, 139–146 (2019).

68. Ravel, B. & Newville, M. ATHENA, ARTEMIS, HEPHAESTUS: data analysis for X-ray absorption spectroscopy using IFEFFIT. *J. Synchrotron Radiat.* **12**, 537–541 (2005).

69. Kresse, G. & Furthmüller, J. Efficient iterative schemes for ab initio total-energy calculations using a plane-wave basis set. *Phys. Rev. B* **54**, 11169–11186 (1996).

70. Kresse, G. & Joubert, D. From ultrasoft pseudopotentials to the projector augmented-wave method. *Phys. Rev. B* **59**, 1758–1775 (1999).

71. Blöchl, P. E. Projector augmented-wave method. *Phys. Rev. B* **50**, 17953–17979 (1994).

72. Perdew, J. P. & Wang, Y. Accurate and simple analytic representation of the electron-gas correlation energy. *Phys. Rev. B* **45**, 13244–13249 (1992).

73. Huang, S.-D., Shang, C., Kang, P.-L., Zhang, X.-J. & Liu, Z.-P. LASP: fast global potential energy surface exploration. *WIREs Comput. Mol. Sci.* **9**, e1415 (2019).

74. Guan, S.-H., Zhang, K.-X., Shang, C. & Liu, Z.-P. Stability and anion diffusion kinetics of yttria-stabilized zirconia resolved from machine learning global potential energy surface exploration. *J. Chem. Phys.* **152**, 094703 (2020).

75. Ma, S., Shang, C., Wang, C.-M. & Liu, Z.-P. Thermodynamic rules for zeolite formation from machine learning based global optimization. *Chem. Sci.* **11**, 10113–10118 (2020).

76. Guan, S.-H., Shang, C., Huang, S.-D. & Liu, Z.-P. Two-stage solid-phase transition of cubic ice to hexagonal ice: structural origin and kinetics. *J. Phys. Chem. C* **122**, 29009–29016 (2018).

77. Huang, S.-D., Shang, C., Zhang, X.-J. & Liu, Z.-P. Material discovery by combining stochastic surface walking global optimization with a neural network. *Chem. Sci.* **8**, 6327–6337 (2017).

78. Behler, J. & Parrinello, M. Generalized neural-network representation of high-dimensional potential-energy surfaces. *Phys. Rev. Lett.* **98**, 146401 (2007).

Acknowledgements

Author contributions

L.T. conceived and designed the experiments. H.Z. performed the catalyst synthesis, characterization and performance experiments. Z.L. and S.M. contributed to the DFT calculation and wrote the related section of the manuscript. R.Y., K.X., Y.C., K.J., Y.F., C.Z. and X.L. assisted with the synthesis and performance testing of the catalysts. Y.T. and L.W. helped to analyse the XPS and XAS data. Q.J. conducted the HAADF-STEM experiments. P.H. and Y.W. assisted with the in situ DRIFT experiments. Data were discussed among all coauthors. L.T. and H.Z. wrote the manuscript.

Competing interests

The authors declare no competing interests.

Additional information